Dalton Transactions

Accepted Manuscript

Volume 45 | Number 1 | 7 January 2016 | Pages 1–398

Dalton Transactions

An international journal of inorganic chemistry
www.rsc.org/dalton

ISSN 1477-9226

ROYAL SOCIETY OF CHEMISTRY

PAPER
Joseph T. Hupp, Omar K. Farha et al.
Efficient extraction of sulfate from water using a Zr–metal–organic framework

175 YEARS

ROYAL SOCIETY OF CHEMISTRY

rsc.li/dalton

Facile synthesis of cationic doped $[Ca_{24}Al_{28}O_{64}]^{4+}.(4e^-)$ composite via rapid citrate sol-gel method

Karim Khan[a]*, Ayesha Khan Tareen[b], Sayed Elshahat[a], Ashish Yadav[a], Usman Khan[c], Minghui Yang[b], Luigi Bibbò[a], Zhengbiao Ouyang[a]*

[a.] College of Electronic Science and Technology of Shenzhen University, THz Technical Research Center of Shenzhen University, Key Laboratory of Optoelectronics Devices and Systems of Ministry of Education and Guangdong Province Shenzhen University, Shenzhen 518060.

[b.] Ningbo Institute of Material Technology and Engineering, Chinese Academy of Sciences, Ningbo, 315201, P. R. China,

[c.] Low dimensional materials and devices laboratory, Tsinghua-Berkeley Shenzhen institute, Tsinghua University Shenzhen, 518055, PR China.

*Corresponding author: zbouyang@szu.edu.cn (Zhengbiao Ouyang), karim_khan_niazi@yahoo.com (Karim Khan)

Abstract: One of the greatest challenge about the enhancement in electrical properties of the conductive mayenite, $[Ca_{24}Al_{28}O_{64}]^{4+}(4e^-)$ (thereafter C12A7:e$^-$) was to design a more suitable/simple synthesis strategy that can be employed to obtain the required properties like excellent stable electrical conductivity, high electron concentration, marvelous mobility and with exceptionally high surface area. Therefore, to synthesize C12A7:e$^-$ with metallic state, we proposed a facile, direct synthesis strategy based on optimized sol-gel combustion method under nitrogen gas environment, using low cost precursors $Ca(NO_3)_2.4H_2O$, and $Al(NO_3)_3.9H_2O$. Based on this developed strategy we successfully synthesized moderate conductive nano-scale C12A7:e$^-$ powder but with unexpected carbon components (Reduced Graphene Oxide (rGO), and/or Graphene Oxide (GO)). The synthesized C12A7:e$^-$ - composite at room temperature has electrical conductivity of about 21 S.cm^{-1}, high-density electron concentrations c.a. 1.5×10^{21} cm^{-3}, and a largest specific surface area of 265 m^2 g^{-1}. Probably the synthesized rGO was coated on nanocage C12A7:e$^-$ particles. Generally, the C12A7:e$^-$ electride is sensitive to the environment (especially to oxygen and moistures), and is protected by rGO coating on C12A7:e$^-$ particles which, also enhance the mobility and keep the conductivity of the C12A7:e$^-$ electride stabile in long time. Doped mayenite electride, exhibits a conductivity strongly dependent on the substitution level, the conductivity of Gallium-doped mayenite electride increases with doping level and has a maximum value of 270 S.cm^{-1} which in first time reported for stable C12A7:e$^-$ electride, and in case of Si-substituted calcium aluminate the conductivity has a maximum value of 222 S.cm^{-1}, at room temperature.

Key words: Synthesis nanosize C12A7:e$^-$composite, Cation doping, highest surface area, moderate conductivity.

INTRODUCTION

Mayenite $12CaO.7Al_2O_3$ (thereafter C12A7) is a typical phase presented in cement, which became well known quite early in concrete research but Lacerda *et al.*,[1] introduced it first time as high oxide conductor. The insulator nature belief of C12A7 was changed in 2002 when Hayashi *et al.*, first time reported its light-induced conversion into conducting mayenite C12A7:e$^-$.[2] Light metal, inorganic, wide bandgap (~7eV), clathrate compound C12A7:e$^-$ is a novel player among the Transparent Conducting Oxides (TCOs) as well as in electride family[3,4], where by controllable way of electron-gas it can change without losing fundamental cage framework structure[5,6], even the filled cages structure remains in high temperature melt and also in glass form[7], as well as under high pressure till GPa
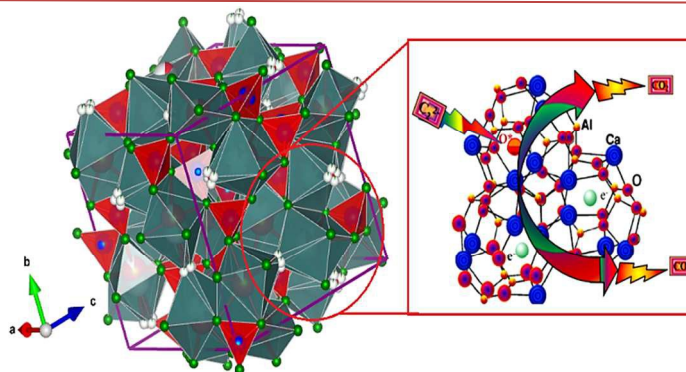
range.[8] The metallic state with highly electron-doped nano-sized cage array of this environmentally-benign low work function porous C12A7:e$^-$ material forms a quantum dot.[9] Synthesizing this material with nano-size may manifest other extremely fascinating, useful properties, which can be exploited for a variety of applications in photoelectron highly functional and effective devices.[10] The academic research on the natural nano-size cage structural C12A7:e$^-$ material, first room temperature stable electride is constantly in progress in developing new fundamental science and their potential industrial applications. The electrochemical reduction of oxymayenite, C12A7 to electron-loaded low work function mayenite C12A7:e$^-$ is a particularly promising means for achieving this aim because of its huge industrial applications. At present, important applications of C12A7:e$^-$ are as a catalysts support[11-14], electron emitter[15], ionic conductor[16-18], superconductor[19,20], and transparent conductive oxide (TCO)[21], making this novel, cheap, environmentally friendly material more attractive. Continuous improvement on its properties and applications is under way, but the complexity of the previous synthesis process of C12A7:e$^-$ has motivated many researchers towards developing direct simple synthesis route because previous methods are based on high energy consumption, long synthesis time with high synthesis temperature, and lower specific surface area. Therefore herein, we focus on the simple step, less energy consumption production of high surface area nanoporous C12A7:e$^-$ with high electron concentration and mobility, to further enhance the potential industrial applications of unusual properties of this novel material.

Oxymayenite C12A7 and mayenite electride C12A7:2e$^-$ have attracted scientific attention as functional materials with high ionic substitution and as conduction material. In contrast, however, less is studied about cationic substitutions. Jian Huang *et al*., theoretically studied about the cation substitution (Mg^{2+}, Cu^{2+}, Sr^{2+}, Fe^{3+}, Ir^{4+}, P^{5+} and V^{5+}) in C12A7 and C12A7:e$^-$ by DFT-method. They studied in detail the influences of cations on the structural and electronic features of C12A7 and its electride variant.[22] Theoretical calculations showed that the cation doping / substitution in C12A7:e$^-$ strongly effects the electrical properties and hence here we studied it experimentally.

The environmental effect, especially the oxygen influence on the low work function (~2.4 eV) conductive C12A7:e$^-$, compared to that of alkaline and alkaline earth metals, can be overcome by coating it with carbon components, like Graphene Oxide (GO), reduced Graphene Oxide (rGO) or Graphene.[23] Similar to the protection of refined metals from reactive environments, C12A7:e$^-$ is also significant to many industrial and academic applications. For protection of metals current methods generally used are, coating with organic layers, paints or varnishes, polymers, formation of oxide layers, anodization, chemical modification, and coating with other metals or alloys. However, all these methods previously used cause numerous negative effects, e.g. increased thickness and changes in the metal physical properties.[23] Usually, the unique electrical / optical / mechanical properties of graphene family with extremely large surface area and low fabrication cost have led to enormous possibilities for innovative applications in novel electronics, optoelectronics, display devices, sensors and next-generation photovoltaic devices but regarding to the environmental protection layer of metals this material becomes more important. General speaking, graphene based research got exceptional scientific and applied industrial interests in a very short period of time since its discovery (2004). Graphene with 2D densely packed

sp^2-bonding carbon atoms in honeycomb arrangement exhibits high conductivity as well as thermal, chemical and mechanical stability. Generally graphene synthesis methods are, mechanical exfoliation, epitaxial growth, chemical vapor deposition and conversion of GO into graphene.[24] However, unexpected graphene based material synthesis in our experiment maybe the next new but facile method for highly crystalline graphene growth scheme and their coating on C12A7:e$^-$ will protect and maintain its long time stable conductivity.

The development of simple, easy steps to synthesis of C12A7:e$^-$ requires breakthroughs because the conventional synthesis techniques have inherent advantages but mostly have limited electrical properties or are restricted to a single crystal under a vacuum preparation methods, exclusive of few methods.[2,25] In the earlier synthesis techniques and investigations, each of those reduction methods requires extreme conditions, but future generations require more efficient, mass productive and generalized synthesis techniques for chemical synthesis of C12A7:e$^-$ with good opto-electrical properties.[4,9,13,26-33] This has stimulated the development of strategies to overcome these drawbacks.[4] Therefore, compared to conventional synthesis of C12A7:e$^-$ herein we report a very simple, less time/energy consuming, cost-effective, single step based, very easy, mass production, and convenient method and it overcomes the limitations in previous methods. By this new method, insulating oxide C12A7 can be converted to nano-size particles with highest surface area, having a different degree of conductivity/crystallinity. Synthesized nanocrystals of C12A7:e$^-$ were used for an initial investigation into its crystalline bulk and nanoparticle form.

EXPERIMENTAL SECTION
Sample synthesis methodology

To synthesize C12A7:e$^-$ via modified sol-gel base synthesis, analytical grade starting materials $Ca(NO_3)_2 \cdot 4H_2O$ (purity 99.0%; Aladdin/Shanghai, China) and $Al(NO_3)_3 \cdot 9H_2O$ (purity 99.0%; Aladdin/Shanghai, China) were used as source materials for CaO and Al_2O_3, respectively. In the first step, metal nitrates of defined weight were weighted ($Ca(NO_3)_2 \cdot 4H_2O : Al(NO_3)_3 \cdot 9H_2O$ = 12:14) and then dissolved in ethylene glycol (EG) $C_2H_6O_2$ (purity 99.0%; Aladdin/Shanghai, China) at 60 °C to get transparent solution. The solution was stirred and in the meantime appropriate amount of citric acid (CA) was added slowly at 60 °C. The ratio of CA to metal cations ($M_{Ca,Al}$) was kept as 1 ($CA/M_{Ca,Al}$ = 1). By using a magnetic stir bar, citrate-nitrate mixture was vigorously stirred at ~80 °C for 6 hours to obtain a clear transparent viscous gel. This gel was kept at about 100 °C for one hour in vaporized physically absorbing water, then dried at 200 °C for 6 hours in a drier to vaporize extra EG, along with starting CA decomposition and finally we got light brown soft-cake like xerox-gel, which was crushed into powder and then divided into two parts, one was pressed in pellet shape at 150 MPa and another was directly used to get a conductive powder. Before further heat treatment, the resulting dried gel powder was further pulverized and both powder and pellets were heat treated at 500 °C for 1hour in a nitrogen environment with 5 °C per minute increase/decrease rate to burn off most of the organic residues and also completely decompose the CA. Finally, the resultant powder and pellets were sintered in an alumina crucible using an nitrogen atmospheric tube furnace, with a temperature program involving constant heating rate of 300 °C/h and maintenance of the temperature at 700 °C, 1000 °C, 1150 °C, and 1550 °C for 1 hour, followed by natural cooling (**Fig. 1**). By successful implementation of the prescribed steps we

have been able to synthesize C12A7:e⁻. In contrast, air/oxygen atmosphere synthesis under the same conditions using an alumina crucible gives us an electrically insulating mayenite, C12A7.[33] In case of

doping, the same synthesis procedure is repeated and source of Si (SiO$_2$, 99.0 %) and of Ga (Ga(NO$_3$)$_3$.9H$_2$O, 99.0 %) were added with starting precursors in molar weight of x = 0.20, 0.50, 0.80, and 1, respectively.
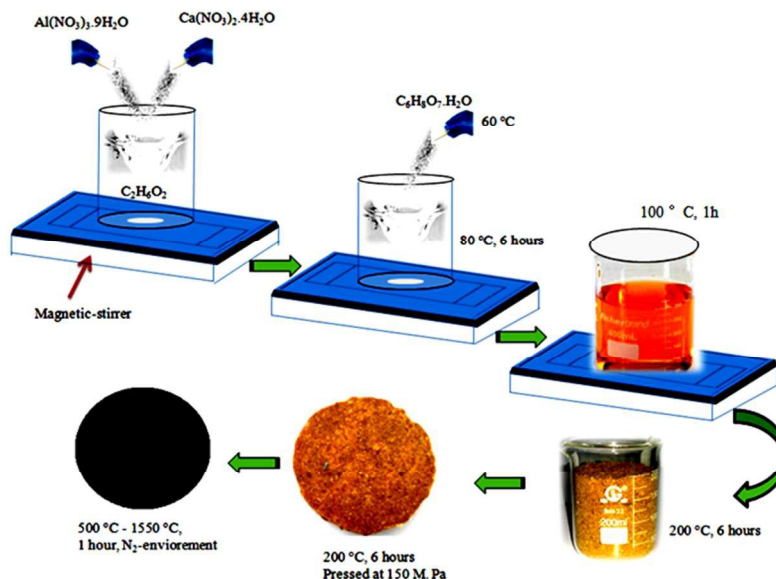

Fig. 1. Schematically diagrammatic illustration of C12A7:e⁻ synthesis process.

CHARACTERIZATION

Under the guidance of the formation mechanism, the synthesized C12A7:e⁻ powder is discussed in detail by consulting different experimental conditions based on the synthetic pathways from precursors to final conductive powder. Possible chemical reactions during sintering and thermal stability after sintering were determined using thermo gravimetric/differential thermal analyses (TG-DTA) (Diamond TG-DTA; Perkin-Elmer instrument (SII) Thermoplus, Rigaku). The influence of sintering temperature on the crystallinity, conductivity and surface area were investigated, which strongly impacts on its final applications. Therefore, X-ray powder diffraction (XRD) technique was used to study the crystallographic phase of heat treated powders, using a D8 Advanced Bruker AXS diffractometer with Cu-Kα radiation source (λ = 0.15406 nm, 40 kV, 360 mA). The electrical conductivity of a sample was measured by four probe method. The Brunauer–Emmett–Teller

(BET) specific surface areas and pore volume/width of the samples were calculated by measurement of nitrogen adsorption–desorption isotherms under liquid nitrogen environment at temperature of -196 °C using an automatic specific surface area and pore physical adsorption analyzer (ASAP) (ASAP 2020, Micrometrics) after evacuation of the samples at 200 °C for 5 hours. To study the microstructure and morphology of sintered powder transmission electron microscopy (TEM) and high-resolution TEM (HRTEM) images were obtained on a JEOL-2100 electron microscope operating at 200 kV. The X-ray photoelectron spectroscopy (XPS) measurement was carried out on an X-ray photoelectron spectrometer (Thermo Scientific, VG Multilab 2000) with Al Kα radiation (hv=1486.6 eV) under UHV (1.33×10⁻⁸ Pa). The energy resolution was set to 0.5 eV for wide scans and 0.05 eV for narrow scans, respectively. The analyzer pass energy was set to 20 eV for narrow scans.

All peaks are calibrated by the carbon deposit C 1s binding energy at 284.8 eV.

RESULTS AND DISCUSSION

Thermal analysis

To know the basic physical and chemical changes in the material properties as a function of increasing temperature at a constant rate, TG/DTA of the gel were performed. The data for the endothermic/exothermic reactions and phase transformation during the mayenite synthesis were collected in nitrogen gas environment from 30 °C to 1250 °C (**Fig. S2**). The important point during this heat treatment process is that, a distinct exothermic peak at 600 ºC in all the samples indicates the oxidization of free extra carbon from incomplete combustion of the citric acid[34] and hence reduction of free oxygen in C12A7. Therefore the basic reason for the non-conductive property of all samples at 500 ºC observed is because no distinct reduction occurs, even there exist free carbon but the sample heat treated at 700 ºC has a distinct value of conductivity and this value of conductivity further increases with increasing synthesis temperature under the same conditions of applied environment and time.

Crystal structure and phase purity of mayenite

Taking into account the above TG/DTA variation trends we select different synthesis temperatures and to study that synthesized mayenite crystallographic phase, XRD technique was used. The gel, heat treated at 500 °C for 1hour in nitrogen environment and obtained as gray ash (AS) which was amorphous in nature and does not indicate any peak of hydroxycarbonate, hydroxyl and carbonate groups, is independent of the decomposition either in a single step or in two steps.[34] When the ash was further calcined at the temperature range of 700 °C to 1000 °C for 1 hour in nitrogen environment, all the calcined products were almost amorphous in nature. Although the XRD patterns of the 700 °C calcined powder in nitrogen environment did not indicate any peaks of carbonate especially crystalline $CaCO_3$ phase, which is observed when we heated the same gels in air environment (supporting data, **Fig. S1(a, b)**), that is also reported previously.[35] The C12A7:e⁻ phase identification and crystallinity, based on XRD illustrate that the first crystalline phase of C12A7:e⁻ was observed at about 1000 °C (**Fig. 2(a)**).[35] The XRD of the samples heat treated at 1150 °C and 1550 °C shows a well-resolved sharp peak in the XRD pattern; corresponding to the well crystalline C12A7 phase (JCPDS, CAS number 09-0413), there is no second impurity phase peak related to CaO and Al_2O_3 family. The reduction treatment did not change the basic structure of the lattice framework of C12A7 with high temperature treatment but the sample color changed from yellow gel to gray ash, and finally to black amorphous/crystalline C12A7:e⁻ phase with an increasing synthesis temperature for the same time duration.
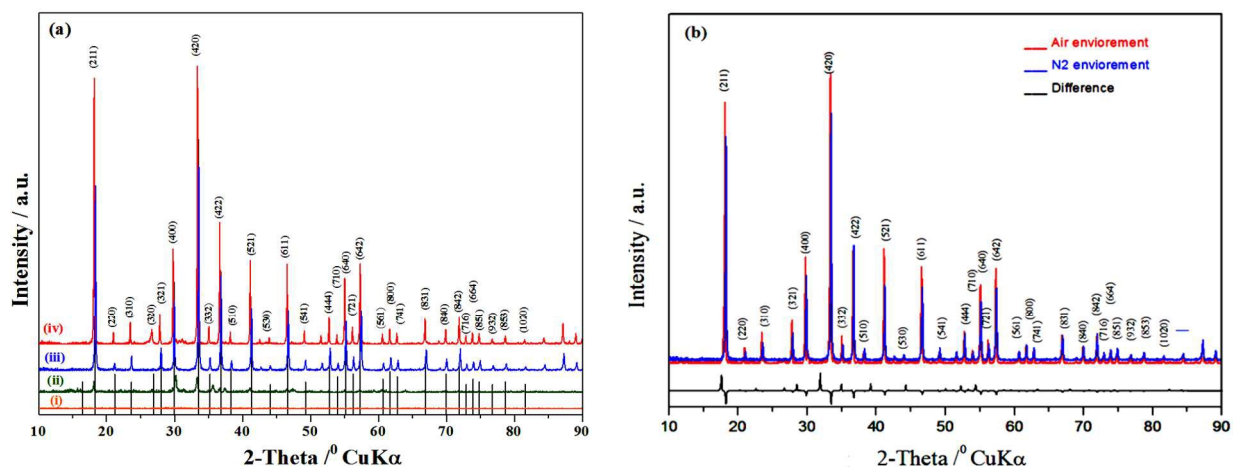
Fig. 2. (a) Observed XRD patterns of synthesized samples at **(i)** 700 °C, **(ii)** 1000 °C, **(iii)** 1150 °C, and **(iv)** 1550 °C. For comparison, the lines on the x-axis correspond to the peak positions for the pure C12A7, **(b)** CA-treated C12A7 in nitrogen and air heat treated, with the bottom line shows the difference between two patterns.

The mean diameter of the particles was estimated by the Scherrer formula from (211) peak and this average crystallite size was about in the range of 5 nm - 10 nm, and is much smaller than the previously reported values based on the sol-gel method ((357.5 nm)[36] and (33–74 nm)[37] and high-temperature gas–solid method (c.a. 170 nm)[37] for insulating C12A7. **Figure 2(b)** shows a decreasing crystallinity of about 20 % after reduction treatment, which is almost the same like previously published results based on simulated and experiments results.[25]

Scanning and Transmission Electron Microscopy (SEM/TEM)

Further we did SEM analysis of the highly conductive C12A7:e⁻ sample synthesized at 1550 ºC, based on our required goal (**Fig. 3**). The micrographs show edge shaped particles and displayed coating with carbon compound, probably rGO. The EDS mapping of the sample heat treated at 1550 °C in N₂-atmosphere showed a homogeneous distribution of the carbon on the powder surface (**Fig. 4**). This coating on the C12A7:e⁻ is further explained by and verified by TEM / high-resolution TEM (HR-TEM) analysis.

Fig. 3. SEM graph of sample heat treated at 1550 °C in N₂-atmosphere.

The TEM and HR-TEM images of dispersed C12A7:e⁻ composite powder (heat treated at 1550 °C) in ethanol for three hours followed by ultrasonication and their Selected Area Electron Diffraction (SAED) pattern (**Fig. 5**) shows the microstructures and crystallinity of synthesized powder. The TEM-images show the well distributed isolated almost spherical type shape C12A7.e⁻ nano sized particles with the average size of ca. 5 nm, without the aggregated precipitates. A number of nano particles in size c.a. 10 nm and also few in 20 nm were observed.
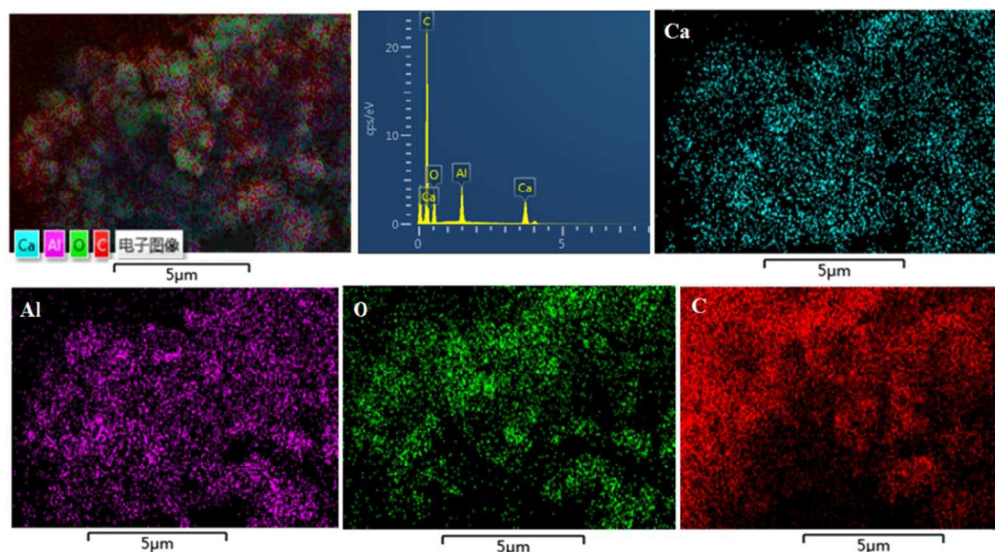
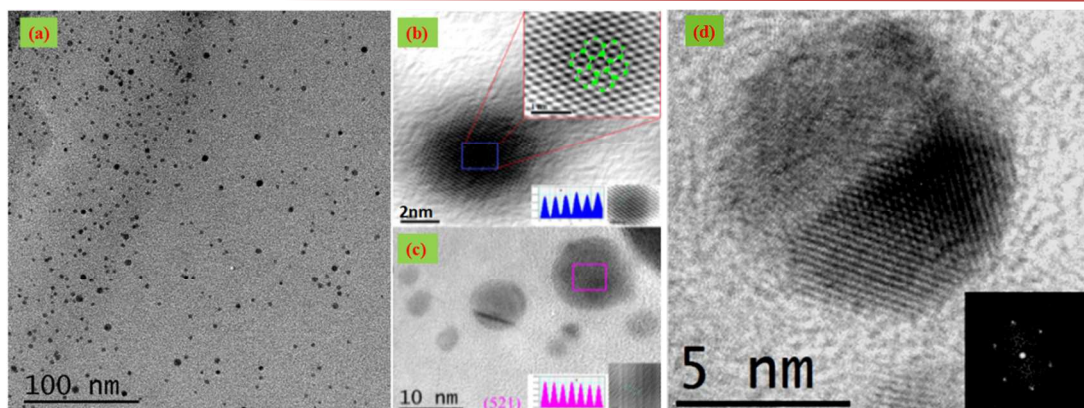**Fig. 4.** Element distribution map (SEM-EDS) of sample heat treated at 1550 °C in N_2- atmosphere.

Fig. 5. (a) TEM, **(b, c, and d)** HR-TEM images, and SAED patterns (insets) of C12A7.e⁻ sample synthesis at 1550 °C.

Figure 5(b) shows the HR-TEM image of the synthesized powder where the layers of rGO are clearly observed and the layers are partly overlapped by each other, hence gives the confirmation of the many layer coating.[38,39] Generally speaking, **Fig. 5(b)** indicates an AB-stacking type of bilayers where only half of the atoms in the upper sheet lies over another atom, whereas the other half lie over the center of a hexagon formed by the atoms in the lower sheet. The well-defined d-spacing in **Fig. 5(c)** corresponds to the C12A7:e⁻ particles and shows the nano-polycrystalline mayenite phase (JCPDS, CAS number 09-0413). Hence, we first time successfully partially synthesized

C12A7:e⁻ powder on nano-size isolated coating powder. As the C12A7:e⁻ conductivity is affected by oxygen and moistures, so this type of coating will prevent C12A7:e⁻ from oxygen / moisture and its conductivity will remain constant for a long time, without any capsulation requirement in its devices fabrication.[23] Hence single step C12A7 reduction and coating has been done. To further study the particle shape we performed HR-TEM analysis. **Figure 5(d)** shows polycrystalline particles, which have an edge shape, and may also contribute to increasing the surface area of C12A7:e⁻.

Raman Spectroscopy

The Raman spectroscopy has historical importance in the investigation and characterization of molecule structure and bonding of the graphitic materials. The Raman spectra were excited by a 532 nm air-cooled argon ion laser (20mW). As displayed in **Fig. 6**, the higher intensity of G-band than that of 2D-band with the position of the G-band peak moving towards the small Raman shift indicated the existence of many layers of graphene family. In addition, a comparatively very weak D band peak (1348 cm^{-1}) emerges in the Raman spectra. The existence of the D band peak suggests that the rGO synthesized is defective. The appearance of both G and 2D band peaks signifies the readily formation of rGO under applied thermal conditions. As the peak intensity ratio I_{2D}/I_G is less than 1 and the FWHM of the 2D band peak is ~88 cm^{-1}, the obtained rGO should be the stacking of multilayer sheets. In this work, generally the small D band peak and high 2D band peak in the Raman spectrum could be ascribed to the excellent reduction of rGO during synthesis process at 1550 °C in a N$_2$ atmosphere, in which the oxygen moieties were removed and the sp^2 network was restored due to structural relaxation.[40] Raman bands located at 200-1000 cm^{-1} were arisen from the lattice framework of C12A7, which was composed of tetrahedrally coordinated Al^{3+} ions. The band at 773 cm^{-1} corresponds to stretching vibrations of Al-O in $[AlO_4]^{5-}$ (symmetric); 510 cm^{-1} is a bending vibrations of Al-O in $[AlO_4]^{5-}$; and 330 cm^{-1} is due to vibrations of Ca[AlO$_4$] and Ca-O.[41] For C$_2^{2-}$ the band normally presented at around 1870 cm^{-1} from the reference spectrum of CaC$_2$, is also not present.[42] The peak between 1137 and 1164 cm^{-1}, which was assigned as the O$_2^-$ stretching mode, was not observed in the sample, indicating the reduction of C12A7 into C12A7:e$^-$. The band at 1128 cm^{-1} was attributed to the stretching mode of the extra framework O$_2^-$ ion, which

was not observed here. The existence of the rGO signal indicated that rGO grew homogeneously on the surface of C12A7:e$^-$ powder.
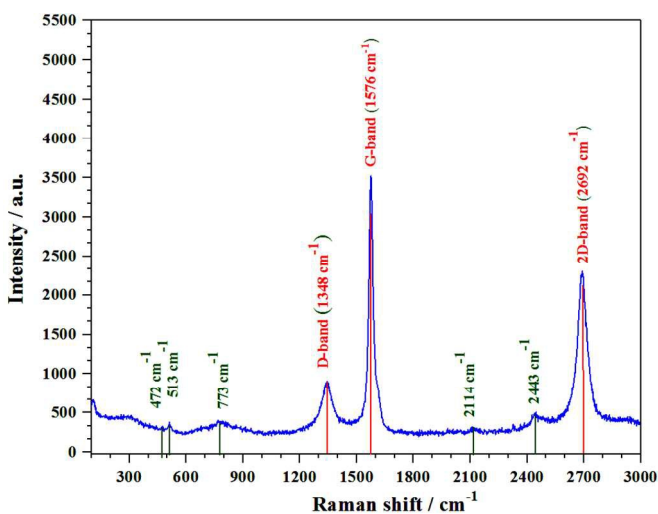

Fig. 6. Raman spectra of the synthesized powder.

X-ray photoelectron spectroscopy (XPS)

X-ray photoelectron spectroscopy (XPS) is a surface-sensitive analytical technique that is useful to determine the chemical environment of atoms. To further improve our understanding of the rGO presence and its affection on the C12A7:e$^-$ properties of materials, XPS measurements were carried out on the powder. Herein, curve fitting of the C$_{1s}$ spectra was performed using a Gaussian–Lorentzian peak shape after performing a Shirley background correction. The wide-scan XPS data of the C12A7:e$^-$ composite powders are provided in **Fig. 7**, where it shows the XPS core level peak spectrum of C12A7 powder, in which Ca, Al, and O can be detected. The stoichiometry verified it well as the nominated C12A7, as calculated from Ca 2p, Al 2p and O 1s peak area amounts.

The C1s XPS spectrum (**Fig. 8(a)**) showed a sharp peak at 284.426 eV, which correspond to non-oxygenated rings and hence it refers to aromatic C–C (47%) bonds of sp^2 carbon atoms in a conjugated honeycomb lattice. Based on this result, it can be stated

that the highest peak ratio of the C–C (47%) bond is due to the formation of the C–C skeleton by the reduction process of the oxygen-containing species. [43,44]
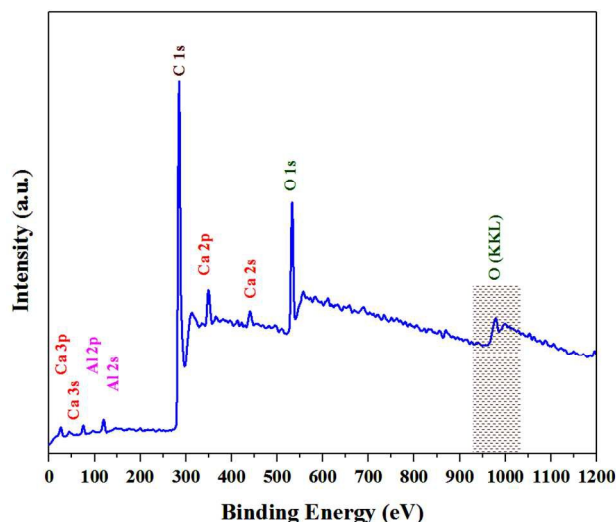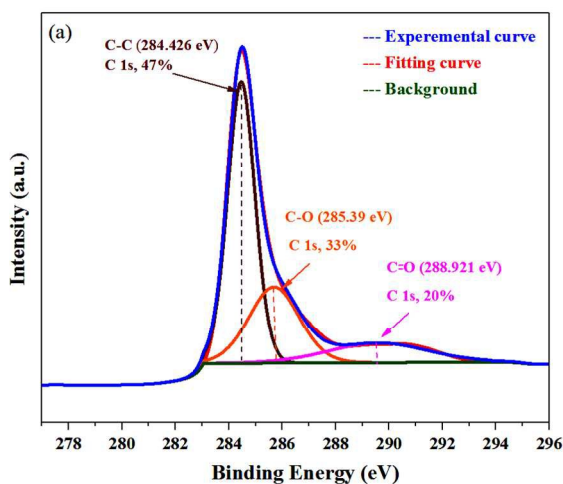

Fig. 7. XPS survey spectra of the final synthesized material at 1550 °C, 1h.

Similarly, oxygenated rings peaks at 285.39 eV, and 288.921 eV could be attributed to the C in C–O or C–

OH (33%), and carbonyl (C=O, 20%), respectively. It can be concluded that the observations described prove that the formation of the rGO, but only to a certain degree. A significant portion of more stable oxygenated functional groups preserved even after the reduction.[43] The C/O ratios determined by XPS had values of ~13.5, which is in close to the amount in chemically produced rGO. [45] **Figure 8** also shows the XPS spectra of O 1s, Ca 2p, and Al 2p, respectively.Ca 2p narrow XPS spectrum in **Fig. 8(b)** has two peaks at around 352.197 eV and 348.544 eV, which are related to Ca $2p_{1/2}$ and Ca $2p_{3/2}$, respectively. Due to spin orbit splitting, the Ca 2p XPS spectrum has clearly distinguishable two peaks. The narrow and sharp peaks indicate that Ca connected with O.[46] The Al 2p XPS spectra in **Fig. 8(c)** have peak positions at around 75.473 eV, indicating that the valence state of Al in C12A7 is the same as that of Al_2O_3. So, we can conclude that only Ca-O bonds and Al-O bonds exist in C12A7:e⁻.
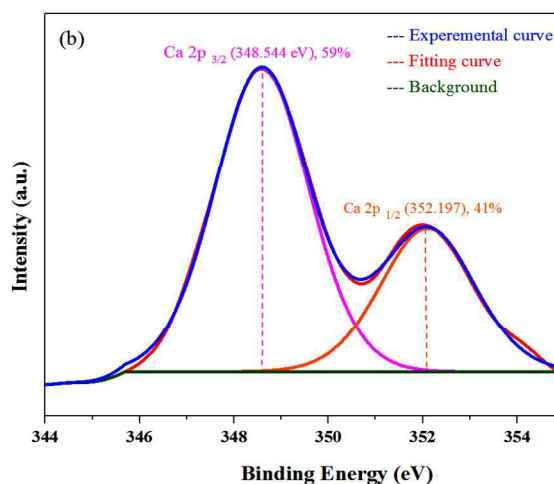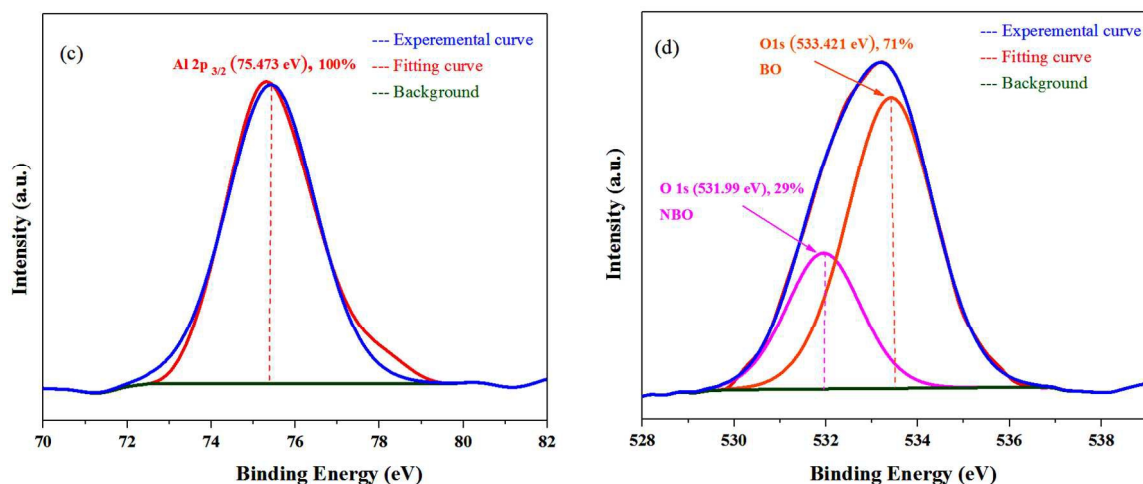
Fig. 8. XPS survey spectra of **(a)** C 1s, **(b)** Ca 2p, **(c)** Al 2p, and **(d)** O 1s.

Table 1. XPS data of C12A7:e⁻ composite.

Element/Transition Peak	Energy (eV)	Peak Width FWHM, (eV)	Peak Area (counts)	Concentration (at. %)
C 1s	284.426	0.886391	2657.7	47%
C 1s	285.39	2.19332	1911.7	33%
C 1s	288.921	5.17973	1181.8	20%
Ca 2p$_{3/2}$	348.544	2.22739	644.4	59%
Ca 2p$_{1/2}$	352.197	2.96415	450.9	41%
Al 2p	75.473	3.05805	192.9	100%
O 1s	533.421	2.40294	1665.7	71%
O 1s	531.952	2.14205	685.9	29%

The O 1s spectrum in **Fig. 8(d)** can be clearly explained as two distinct contributions, whose peaks are at around 531.99 eV and 533.421 eV, respectively. The high energy component is attributed to bridging oxygen (BO) atoms, while the low energy component is assigned to non-bridging oxygen (NBO) atoms.[46] **Table 1** provides an analysis of the spectrum peaks, showing the most probable origin of the peaks with their binding energies and atomic percentage of each group.

Brunauer Emmett Teller calculations

BET theory is based on the physical adsorption-desorption of gas molecules on a solid surface by which the specific surface area of that material is calculated. The estimated BET specific surface area of the resulting samples (**Fig. 9**) heat treated at 700 °C , 1000 °C , 1150 °C and 1550 °C were 26 m² g⁻¹, 28 m² g⁻¹, 153 m² g⁻¹, and 265 m² g⁻¹, respectively. The variation trend in the surface area with temperature by this method is completely opposite than previously studied reduction method based synthesis of C12A7:e⁻.[12] The reason maybe that the rGO coating on particles does not allow the particles to agglomerate, acquiring nanosized

particles as well as further reducing it. While far from record-high values, the increasing trend in surface area of the nano-material C12A7:e⁻ with the largest surface area value of ca. 265 m^2 g^{-1} is much higher than that of prepared C12A7:e⁻ based on conventional solid-state reaction method (ca. 1 m^2 g^{-1})[12] and hydrothermal method (8-24 m^2 g^{-1}). [47,48] The pore size distribution calculated by the BJH method from adsorption branches for the mesoporous C12A7:e⁻ sample heat treated at 1550 °C (**Fig. 9a**), reveals that there is a single sharp peak at about 2.7 nm, suggesting that the sample possesses one but uniform pore size distribution of about 2.7 nm. **Figure 9(b)** shows its N$_2$ adsorption–desorption profiles, where P is the partial pressure of the adsorbate and the P_0 is adsorbent saturated vapor

pressure. The N$_2$ isotherm is a type IV isotherm and higher N$_2$ adsorption is seen for the sample heat treated at 1550 °C, confirming that it has a larger surface area.[49] The larger surface area may means that the enhancement appears to come from a decrease in particle size and increasing pore size of the nano-size porous C12A7:e⁻ particles, as well as the edge shape of the particles, as can be clarified from the HR-TEM images. This smallest nanosize along with highest surface area will further enhance the future application of this material as a catalyst support material, especially in NH$_3$ synthesis/deposition, and CO$_2$ decomposition and electrode applications. Prior to this report no method for determining such a large surface area for C12A7:e⁻ material has yet been reported.
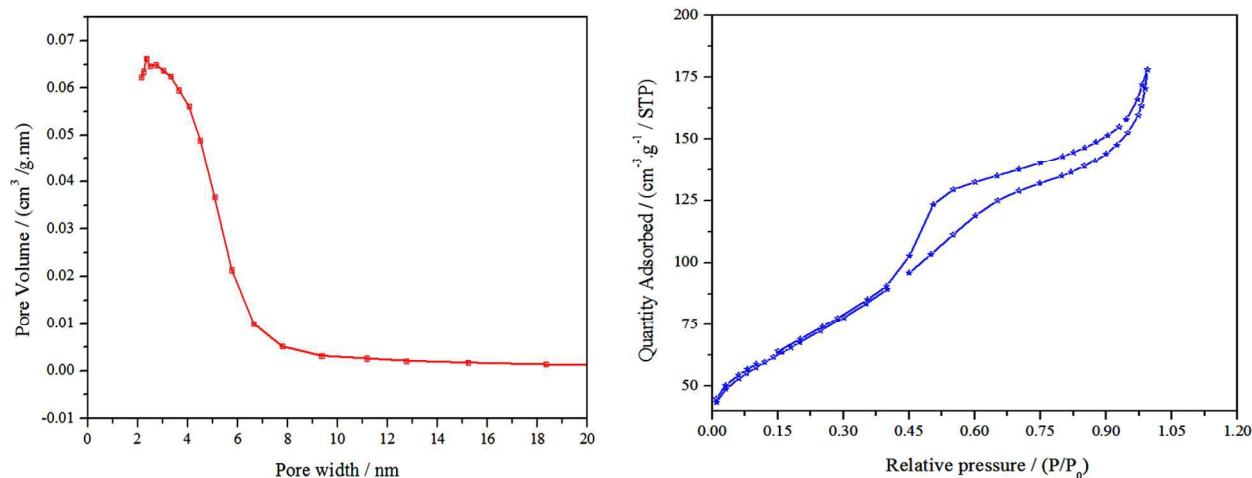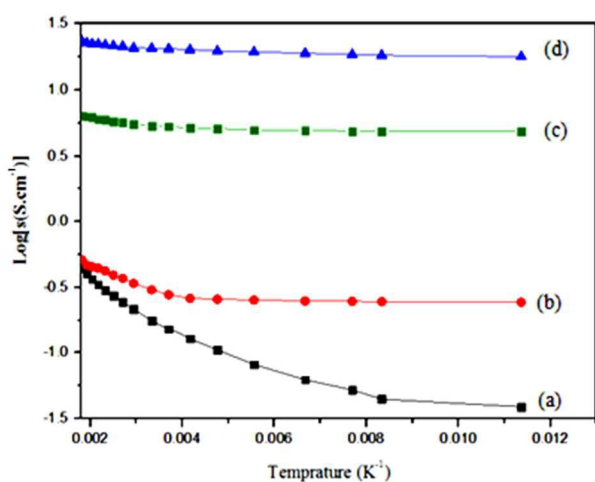

Fig. 9. (a) BJH pore size distributions, **(b)** N$_2$ adsorption/desorption isotherms of 1550 °C sample.
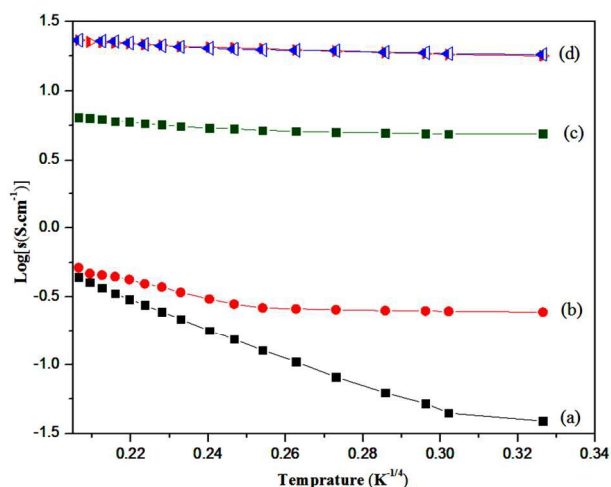
Conductivity variation with temperature

An understanding of charge transport in these materials is essential for research as well as industrial applications. Solid material conduction is sensitive to their crystal structure as well as composition, therefore it is complementary to investigate the conductivity and stability of mayenite under well-defined thermo-dynamic conditions like, preparation method, sintering time, type of applied sintering environment, and sintering temperature.[17] Our attention was focused on the conductivity–temperature characteristics variation,

therefore, the electrical properties of samples sintered at 700 °C, 1000 °C, 1150 °C, and 1550 °C**,** with variable temperature ranging from 90 K to 500 K, were measured using Pt-electrodes formed in a 4-prob configuration (**Fig. 10(a, b)**). The electrical contacts were improved on the sample with the platinum conduction paste. After adjusting a sample the vacuum pump was connected with a chamber and temperature was controlled by Liquid nitrogen (LN$_2$) and thermocouple. The conductivity of the all insulating C12A7 samples heat treated in the air was lower than

Dalton Transactions Accepted Manuscript

the detection limit (10^{-10} S.cm^{-1}) at room temperature. After the heat treatment of the xerox-gel pressed in the pellet form, in the N_2 gas atmosphere for 1 hour at a temperature 600 °C, 700 °C, 1000 °C, 1150 °C, and 1550 °C, the conductivity increased. As the presence of large quantity of water in our precursors causes a possibility of existing OH$^-$ ions in cages, there are more stable substitutive anions, till temperature c.a. 600 °C and it causes a decrease in conductivity.[12] Therefore, a clear conductive behavior in sample was observed at about 700 °C. The plot of the electrical conductivities (**Fig. 10(a)**) shows that for the low-conductivity C12A7:e$^-$ sample synthesized at 700 °C, the log(σ) is

proportional to T^{-1}, showing a semiconducting nature.[33] In the medium-conductivity C12A7:e$^-$ samples heat treated at 1000 °C, and 1150 °C, log(σ) is not proportional to T^{-1} but to $T^{-1/4}$ over a wide range of 90 to 500 K, suggesting the "polaron" nature of electrons.[33] This characteristic implies that the conduction is controlled by a mechanism similar to the variable-range hopping.[50] It is likely that F-like centers are randomly distributed if their concentration is moderately high, and they migrate through the distribution of the potential with varied hopping distances.[50]

(a)

(b)

Fig. 10. Log(σ) (σ, conductivity) vs. 1/ Temperature (T^{-1}, $T^{-1/4}$ (K)) graph of samples synthesis at, (a) 700 °C, (b) 1000 °C, (c) 1150 °C, and (d) 1550 °C.

In the high-conductivity C12A7:e$^-$ sample synthesized at 1550 °C, log(σ) conductivity is almost constant, showing that it is insensitive to the temperature in the range of 90 K to 500 K and perform a metallic conduction. For the C12A7:e$^-$ sample synthesized at 1550 °C, the maximum value of conductivity was about 21 S.cm^{-1} at 300 K, demonstrating that the crystalline C12A7:e$^-$ behaves as metallic conductor and got same value of conductivity after long time exposure to air/moisture **(Fig. 10(b))**. These results of the C12A7 reduction suggest that the

electrons are injected in the C12A7 lattice by this synthesis method by EG+CA treatment by formation of introduced electrons in place of the free O^{2-} ions in C12A7 and rGO composite. We attribute the qualitative synthesis capability of C12A7:e$^-$ to moderate conductivity and hence it shows increasing trend with increasing synthesis temperature until completion of the reduction to the maximum limit of electrons concentration of 1.5×10^{21} cm^{-3}.

CATIONS SUBSTITUTION AND CRYSTALLINE PHASE AND CONDUCTIVITY ANALYSIS

Dalton Transactions Accepted Manuscript

Gallium-doped mayenite electride

To study the improvement in conductivity by controllable substitution of Ga in C12A7 ($Ca_{12}Al_{14-x}Ga_xO_{33+x}$ with x=0. 0.20, 0.40, 0.60, 0.80, and 1), and its reduction we use citrated sol-gel method. Ga-doped C12A7:e⁻ were synthesized in single step and first time we got its stable electride phase, which was previously studied and was reported that gallium-doped C12A7 electride is very difficult to synthesize, if possible.[51] **Figure 11** shows the XRD of the Ga-doped mayenite composite with different ratios, showing first time the successful synthesis of the Ga-doped mayenite electride composite. Previously reported that instead of reduction of Ga-doped C12A7 to Ga-doped C12A7:e⁻, the Ga-doped mayenite undergoes decomposition on reduction to $Ca_3Al_2O_6$ and amorphous Ga metal, which is likely deposited on the mayenite crystal surfaces.[51] Hence we got pure phase till Ga doping level of about x = 1.
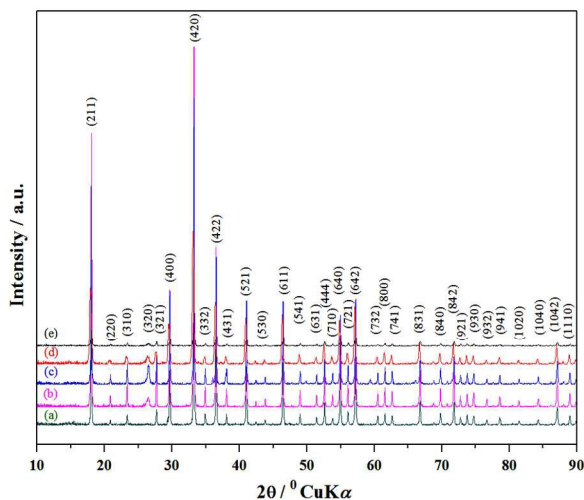

Fig. 11. Observed XRD patterns of Ga-doped C12A7:e⁻ samples synthesized at 1550 °C, with doping quantities, x = **(a)** 0.20**(b)** 0.40, **(c)** 0.60,**(d)**0.8 and **(d)** 1.

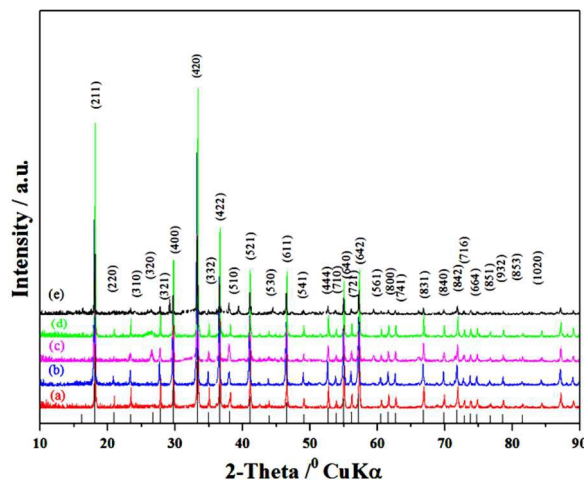**Fig. 12.** Observed XRD patterns of Si-doped C12A7:e⁻ samples synthesized 1550 °C, with doping quantities, x = **(a)** 0.20**(b)** 0.40, **(c)** 0.60,**(d)**0.8 and **(d)** 1.

Si-substituted calcium aluminate

The isovalent Al/Si substitution in mayenite has been studied by preparing the $(Ca_{12}Al_{14-x}Si_xO_{32})O_1\square_5$ series, where,$\square$ stands for an empty site. Single phase compounds can be prepared up to x = 1. The results showed that Si substitutes Al, which provokes the expansion of the unit cell, as expected. **Figure 12** shows Si-doped mayenite composite with different ratios. Hence we got pure phase till Si doping level of about x = 1.
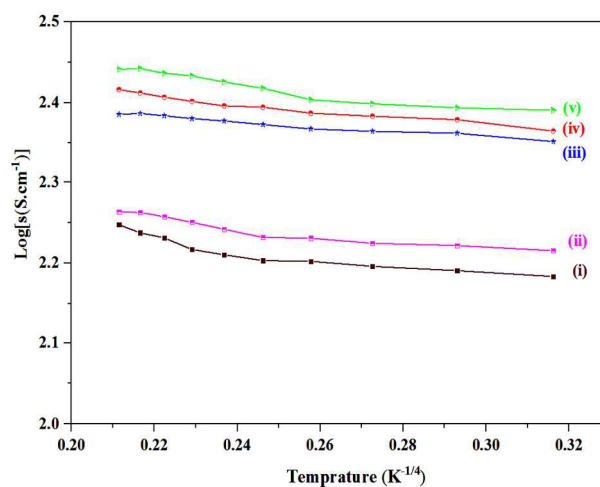

Fig. 13. Log(σ) (σ, conductivity) vs. 1/ temperature(K⁻¹ᐟ⁴) graph of Ga-doped C12A7:e⁻ synthesized at 1550 °C, where x =**(i)** 0.2, **(ii)** 0.40, **(iii)** 0.60, **(iv)** 0.8, and **(v)** 1.
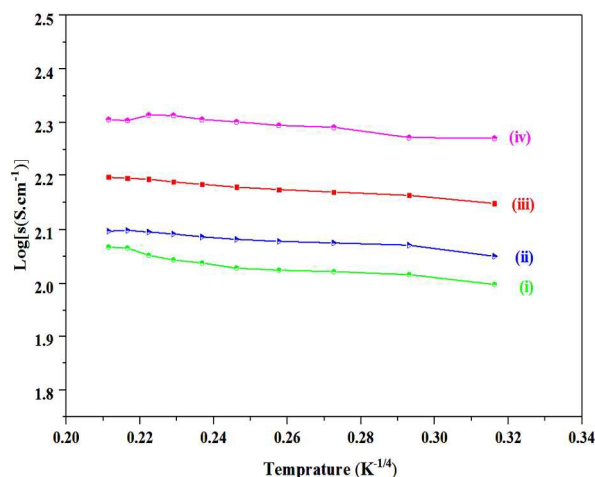
Fig. 14. Log(σ) (σ, conductivity) vs. 1/ temperature ($T^{-1/4}$), (K)) graph of Si-doped C12A7:e⁻, synthesized at 1550 °C, where x =**(i)** 0.2, **(ii)** 0.40, **(iii)** 0.80, and **(iv)** 1.

Conductivity variation with doping level

Gallium-doped mayenite electride, exhibits a conductivity strongly dependent on the substitution level and conductivity increases from 169 S.cm⁻¹, 175 S.cm⁻¹, 239 S.cm⁻¹, 249 S.cm⁻¹, to 270 S.cm⁻¹ as x increases from 0.20, 0.40, 0.60, 0.8 and 1, respectively, at room temperature (**Fig. 13**). In case of the Si-substituted calcium aluminate the conductivity increases from 75 S.cm⁻1, 125 S.cm⁻¹, 167 S.cm⁻¹, to 222 S.cm⁻¹ as x increases from 0.20, 0.40, 0.8 and 1, respectively, at room temperature (**Fig. 14**) and the observed conductivity increasing behavior is consistent with the predictions based on the DFT calculations.[52]

CONCLUSIONS

Here we presented a general strategy and provided a first demonstration of the straightforward synthesis of a novel nanocrystalline C12A7:e⁻ and that doped with Si/Ga cations, without the limitations of type, shape and size (which is synthesized in powder and bulk forms of any size and quantity) and with yielding rGO as byproduct on the surface of the C12A7:e⁻ powder, from precursor $Ca(NO_3)_2.4H_2O$ and $Al(NO_3)_3.9H_2O$, by

using very simple, cheap optimize citrate sol-gel method. The stable mayenite phase is achieved because of the C_2^{2-} template anion, instead of O^{2-} anions in inert gas atmosphere, which also contribute to the reduction process. The TEM based microstructural analysis of the C12A7:e⁻ powder indicates almost isolate, uniform particle distributions. Foremost, this provides a very simple method for mass-production of novel C12A7:e⁻ material at a moderate temperature in an inert gas environment with large surface area (265 m² g⁻¹), where high electrical conductivity (21 S.cm⁻¹) with maximum electrons concentration (c.a. 1.5×10^{21} cm⁻³) will strongly help on large scale potential applications. The synthesized particle surface area was larger than that of previously reported values based on conventional solid-state reaction method (c.a. 1 m² g⁻¹) and hydrothermal method (c.a. 12 m² g⁻¹ – 24 m² g⁻¹). Gallium-doped mayenite electride conductivity increases with doping level to a maximum value of 270 S.cm⁻¹, and in case of the Si-substituted calcium aluminate the conductivity increases to a maximum value of 222 S.cm⁻¹, at room temperature.

This method is based on a scheme without requiring high vacuum, expensive metals, polishing and post-polished rapid-thermal-annealing treatment for restoring the surface cage-structure. In addition, the flexibility associated with this approach of synthesizing the unique cage structure, high specific surface area and outstanding electrical and optical properties of C12A7:e⁻ should enable many applications and also present the opportunity for future studies of doping C12A7:e⁻ with other suitable elements for optimizing its electrical properties. For additional future opportunities we believe that this development of low-temperature simple route will be an open area for researchers to achieve a high mobility, high conductivity, and transparency for flexible electronics

and photovoltaic applications. It would be more interesting to see to what further extent in the catalyst applications behavior of C12A7:e⁻ will be enhanced.

CONFLICT OF INTEREST The authors declare no conflict of interest.

REFERENCES

1 Lacerda, M., Irvine, J. T. S., Glasser, F. P. & West, A. R. High oxide ion conductivity in $Ca_{12}Al_{14}O_{33}$. *Letters to Nature* **332**, 525 - 526 (1988).

2 Hayashi, K., Matsuishi, S., Kamiya, T., Hirano, M. & Hosono, H. Light-induced conversion of an insulating refractory oxide into a persistent electronic conductor. *Letters to Nature* **419**, 462-465 (2002).

3 Ebbinghaus, S. G., Krause, H. & Syrowatka, F. Floating Zone Growth of Large and Defect-free Ca12Al14O33 Single Crystals. *American Chemical Society* **13**, 2990−2994 (2013).

4 Palacios, L. *et al.* Crystal Structures and in-Situ Formation Study of Mayenite Electrides. *Inorganic chemistry* **46**, 4167-4176 (2007).

5 Sushko, P. V., Shluger, A. L., Hirano, M. & Hosono, H. From Insulator to Electride: A Theoretical Model of Nanoporous Oxide $12CaO.7Al_2O_3$. *Journal of american chemical socity* **129**, 942-951 (2007).

6 Kim, S. W., Shimoyama, T. & Hosono, H. Solvated Electrons in High-Temperature Melts and Glasses of the Room-Temperature Stable Electride $[Ca_{24}Al_{28}O_{64}]^{4+} 4e^-$ *Science* **333**, 71-74 (2011).

7 Kim, S. W., Shimoyama, T. & Hosono, H. Solvated Electrons in High-Temperature Melts and Glasses of the Room-Temperature Stable Electride $[Ca_{24}Al_{28}O_{64}]^{4+} 4e^-$. *Science* **333**, 71-74 (2011).

8 Zhang, X. *et al.* Pressure-induced amorphization in mayenite ($12CaO·7Al_2O_3$). *The Journal of Chemical Physics* **135**, 094506-094501-094506-094505 (2011).

9 Kim, S. W. *et al.* Metallic State in a Lime−Alumina Compound with Nanoporous Structure. *Nano letters* **7**, 1138-1143 (2007).

10 Kumar, S. S., Venkateswarlu, P., Rao, V. R. & Rao, G. N. Synthesis, characterization and optical propertiesof zinc oxide nanoparticles. *International Nano Letters* **3**, 1-6 (2013).

11 Chae, H. K. *et al.* A route to high surface area, porosity and inclusion of large molecules in crystals. *Letters to Nature* **427**, 523-527 (2004).

12 Inoue, Y. *et al.* Highly Dispersed Ru on Electride $[Ca_{24}Al_{28}O_{64}]^{4+}(e^-)_4$ as a Catalyst for Ammonia Synthesis. *ACS Catalyst* **4**, 674−680 (2014).

13 Toda, Y. *et al.* Activation and splitting of carbon dioxide on the surface of an inorganic electride material. *Nature communications*, 1 - 8 (2013).

14 Hayashi, F. *et al.* Ammonia decomposition by ruthenium nanoparticles loaded on inorganic electride C12A7:e⁻. *Chemical Science* **4**, 3124–3130 (2013).

15 YashitakeToda *et al.* Field emission of electron anions clathrated in subnanometer sized cages in $[Ca_{24}Al_{28}O_{64}]^{+4}$. (4e⁻). *Advance Material* **16**, 685-689 (2004).

16 Song, C. *et al.* Atomic Fluorine Anion Storage Emission Material C12A7-F and Etching of Si and SiO_2 by Atomic Fluorine Anions. *Chemistry of Materials* **20**, 3473–3479 (2008).

17 Eufinger, J.-P., Schmidt, A., Lerchb, M. & Janek, J. r. Novel anion conductors – conductivity, thermodynamic stability and hydration of anion-substituted mayenite-type cage compounds C12A7:X (X = O, OH, Cl, F, CN, S, N). *Physical Chemistry and Chemical Physics* **17**, 6844--6857 (2015).

18 Schmidt, A. *et al.* Chlorine ion mobility in Cl-mayenite ($Ca_{12}Al_{14}O_{32}Cl_2$): An investigation combining high-temperature neutron powder diffraction, impedance spectroscopy and quantum-chemical calculations. *Solid State Ionics* **254**, 48–58 (2014).

19 Tanaka, S. *et al.* Strong Enhancement of Superconductivity in Inorganic Electride $12CaO·7Al_2O_3.e^-$ under High Pressure. *Journal of the Korean Physical Society* **63**, 477 - 480 (2013).

20 Miyakawa, M. *et al.* Superconductivity in an Inorganic Electride $12CaO 7Al_2O_3:e^-$. *Journal of American Chemical Society* **129**, 7270-7271 (2007).

21 Medvedeva, J. E. & Freeman, A. J. Combining high conductivity with complete optical transparency: A band-structure approach. *Europhysics Letters* **69**, 583-587 (2005).

22 Huang, J., Valenzano, L. & Sant, G. Framework and Channel Modifications in Mayenite (12CaO•7Al2O3) Nanocages By Cationic Doping. *Chemistry of Material* **27**, 4731-4741 (2015).

23 Chen, S. *et al.* Oxidation Resistance of GrapheneCoated Cu and Cu/Ni Alloy. *ACS Nano* **5**, 1321–1327 (2011).

24 JinhaiMao *et al.* Realization of a tunable artificial atom at a supercritically charged vacancy in graphene *Nature Physics* **12**, 545-549, doi:10.1038/NPHYS3665 (2016).

25 Matsuishi, S. *et al.* High-density electron anions in a nanoporous single crystal: $[Ca_{24}Al_{28}O_{64}]^{4+}(4e^-)$. *Science* **301**, 626-629 (2003).

26 Kim, S.-W., Hayashi, K., Hirano, M. & Hosono, H. Electron Carrier Generation in a Refractory Oxide 12CaO. 7Al$_2$O$_3$ by Heating in Reducing Atmosphere: Conversion from an Insulator to a Persistent Conductor. *Journal of American Ceramice Socity* **89** 3294–3298 (2010).

27 Kim, S. W. *et al.* Fabrication of room temperature-stable 12CaO • 7AI$_2$O$_3$ electride: A review. *Journal of Material Science* **18**, S5-S14 (2007).

28 Toda, Y. *et al.* Field emission of electron anions clathrated in subnanometer-sized cages in $[Ca_{24}Al_{28}O_{64}]^{4+}(e^-)$ *Advance Material* **16**, 685-689 (2004).

29 Miyakawa, M. & Hirano, M. High electron doping to a wide band gap semiconductor 12CaO·7Al$_2$O$_3$ thin film. *Applied physics letter* **90**, 182105-182101-182105-182103 (2007).

30 Toda, Y. *et al.* Work Function of a Room-Temperature, Stable Electride $[Ca_{24}Al_{28}O_{64}]^{4+}(e^-)_4$. *Advance Material* **19**, 3564-3569 (2007).

31 Ginley, D. S., Hosono, H. & Paine, D. C. Handbook of Transparent Conductors. *Springer New York Heidelberg Dordrecht London* **1**, 1-536 (2010).

32 Kim, K.-B. *et al.* Photoelectron Spectroscopic Study of C12A7:e and Alq3 Interface: The Formation of a Low Electron-Injection Barrier. *Journal of Physical Chemistry C* **111**, 8403-8406 (2007).

33 Kim, S. W., Toda, Y., Hayashi, K., Hirano, M. & Hosono, H. Synthesis of a room temperature stable 12CaO • 7AI$_2$O$_3$ electride from the melt and its application as an electron field emitter. *Journal of Chemical Materials* **18**, 1938-1944 (2006).

34 Li, J., a, Y. P., Qiu, F., Wu, Y. & Guo, J. Nanostructured Nd:YAG powders via gel combustion: The influence of citrate-to-nitrate ratio. *Ceramics International* **34** 141–149 (2008).

35 Ude, S. N. *et al.* High temperature X-ray studies of mayenite synthesized using the citrate sol–gel method. *Ceramics International* **40**, 1117–1123 (2014).

36 OZAWA, K., SAKAMOTO, N., WAKIYA, N. & SUZUKI, H. Fabrication of 12CaO·7Al$_2$O$_3$ powders with high specific surface area by sol–gel and ball-milling method. *Journal of the Ceramic Society of Japan* **119** 460-463 (2011).

37 Gong, L. *et al.* Synthesis and characteristics of the C12A7-O$^-$ nanoparticles by citric acid sol–gel combustion method. *Materials Letters* **64**, 1322–1324 (2010).

38 Dyck, D. V., Jinschek, J. R. & Chen, F.-R. 'Big Bang' tomography as a new route to atomic-resolution electron tomography. *Letters to Nature* **486**, 243-260 (2012).

39 Huang, P. Y. *et al.* Grains and grain boundaries in single-layer graphene atomic patchwork quilts. *Letters to Nature* **469**, 389-392 (2011).

40 Ren, i.-G. *et al.* A silicon nanowire–reduced graphene oxide composite as a high-performance lithium ion battery anode material *Nanoscale* **6**, 3353 (2014).

41 GALUSKIN, E. V. *et al.* A reinvestigation of mayenite from the type locality, the Ettringer Bellerberg volcano near Mayen, Eifel district, Germany. *Mineralogical Magazine* **76** 707–716 (2012).

42 Kim, S. *et al.* Simple and Efficient Fabrication of Room Temperature Stable Electride: Melt-Solidification and Glass Ceramics. *Journal of American Chemical Society* **127**, 1370 -1371 (2005).

43 Han, N. *et al.* Improved heat dissipation in gallium nitride light-emitting diodes with embedded graphene oxide pattern. *Nature communications* **4**, 1-8, doi:DOI: 10.1038/ncomms2448 |www.nature.com/naturecommunications (2013).

44 Chanda, D. *et al.* The effect of surface modification by reduced graphene oxide on the electrocatalytic activity of nickel towards the hydrogen evolution reaction. *Physical Chemistry Chemical Physics* **17**, 26864--26874 (2015).

45 Sagar, R. U. R., Stadler, F. J., Namvari, M. & Navale, S. T. Synthesis of scalable and tunable slightly oxidized graphene via Chemical Vapor Deposition. *Journal of Colloid and Interface Science* **490**, 844–849, doi:http://dx.doi.org/10.1016/j.jcis.2016.11.073 (2016).

46 Pan, R. K., Feng, S. & Tao, H. Z. XPS and NMR analysis on 12CaO·7Al2O3. *IOP Conf. Series: Materials Science and Engineering* **167** 012017, doi: doi:10.1088/1757-899X/167/1/012017 (2017).

47 Hayashi, F., Kitano, M., Yokoyama, T., Hara, M. & Hosono, H. Surface Treatment for Conductive 12CaO·7Al$_2$O$_3$ Electride Powder by Rapid Thermal Annealing Processing and Its Application to Ammonia Synthesis. *ChemCatChem* **6**, 1317 – 1323 (2014).

48 Li, C., Hirabayashi, D. & Suzuki, K. Synthesis of higher surface area mayenite by hydrothermal method. *Materials Research Bulletin* **46** 1307–1310 (2011).

49 Ranjbar, A. & Rezaei, M. Low temperature synthesis of nanocrystalline calcium aluminate compounds with surfactant-assisted precipitation method. *Advanced Powder Technology*, 1-5 (2013).

50 Matsuishi, S. *et al.* High-Density Electron Anions in a Nanoporous Single Crystal: $[Ca_{24}Al_{28}O_{64}]^{+4}(4e^-)$. *science* **301**, 626-629 (2003).

51 Palacios, L., Bruque, S. & Aranda, M. A. G. Structure of gallium-doped mayenite and its

reduction behaviour *phys. stat. sol. (b)* **245**, 666-672, doi:10.1002/pssb.200743425 (2008).

52 Mariana I. Bertoni, T. O. M., Julia E. Medvedeva, Yongqiang Wang, Arthur J. Freeman, Kenneth R. Poeppelmeier. Enhanced electronic conductivity in Si-substituted calcium aluminate. *Journal of applied physics* **102**, 113704-113701-   113704-113707 (2007).